RSC Advances

PAPER

Cite this: *RSC Adv.*, 2016, **6**, 47258

On the origins of the elasticity of cellulose nanofiber nanocomposites and nanopapers: a micromechanical approach

F. Martoïa,[abcde] P. J. J. Dumont,†*[abc] L. Orgéas,[de] M. N. Belgacem[abc] and J.-L. Putaux[fg]

Cellulose nanofibrils (NFCs) are slender nanoparticles with outstanding mechanical properties that are used to enhance the mechanical properties of polymer nanocomposites and to fabricate dense and transparent nanopapers. However, the reinforcing effect of these nanoparticles is not as efficient for the elastic properties as expected from the classical models for polymer composites or fibrous materials. In this study, nanocomposite films made of TEMPO-oxidized NFCs and polyethylene oxide (PEO) were prepared by varying the NFC content over a wide range. The structural properties of these materials were characterized using AFM, TEM, SEM-FEG and XRD. These techniques showed that NFC nanocomposite films and nanopapers consisted of dense networks of tortuous NFCs with planar and random orientations. DMA experiments also revealed that the cohesive bonds between NFCs greatly contributed to the overall elastic response of these nanocomposites, even for low NFC contents. Based on these observations, we report an original multiscale network model that describes the elastic properties of NFC nanocomposites and nanopapers where the governing deformation mechanisms occurred at the numerous bonds between NFCs and in the NFC kinked regions, whereas the crystalline NFC regions were considered to be rigid bodies. This approach led to the formulation of an analytical expression for the stiffness tensors of NFC nanocomposites and nanopapers and revealed the effects of the network structure on their mechanical responses. The model predictions were satisfactory over the range of investigated NFC contents. In particular, this model showed the predominant role of the amorphous regions on the elastic response, whereas the contribution of the NFC–NFC bonds became significant at high NFC contents.

Received 18th March 2016
Accepted 4th May 2016

DOI: 10.1039/c6ra07176g

www.rsc.org/advances

1 Introduction

Polymer nanocomposites[1–6] reinforced with cellulose nanofibrils (NFCs) as well as dense and transparent NFC nanopapers[7–10] have received considerable attention over the last ten years. One of the main reasons for the growing interest in utilizing NFCs as reinforcing nanoparticles in composites stems from the possibility of exploiting both their outstanding intrinsic mechanical properties and their pronounced slenderness ($100 < l/d < 500$). These emerging biobased nanomaterials, often produced in the form of films, have great potential in a wide variety of applications, such as electronics[8,11,12] and packaging.[10,13,14]

NFCs are renewable semicrystalline nanofibers that are the main reinforcing constituents of plant cell walls.[15] They are commonly isolated from cellulosic fibers using a combination of chemical and mechanical treatments.[2,16] The most commonly used pre-treatment to obtain suspensions of well-individualized NFCs is TEMPO-mediated oxidation of cellulose fibers.[17,18] This pre-treatment preserves the crystalline structure of cellulose and introduces negatively charged carboxyl groups on the fibril surface, resulting in homogeneous and electrostatically stabilized aqueous colloidal suspensions.[17–19] The resulting NFC suspensions usually contain a very large amount of slender individualized nanofibrils with a mean diameter that ranges between 3 and 5 nm and a mean length that ranges between 1 and 1.5 μm.

When they are well-dispersed in polymer matrices, NFCs provide a considerable reinforcing effect, even at very low volume fractions.[1,20,21] In general, NFC-reinforced polymers exhibit a drastic increase in both their elastic and plastic properties.[1,3] This reinforcing effect is often preserved up to 500 K, *i.e.*, the temperature at which cellulose decomposes.[1,22] This

[a]*Univ. Grenoble Alpes, LGP2, F-38000 Grenoble, France. E-mail: pierre.dumont@insa-lyon.fr*
[b]*CNRS, LGP2, F-38000 Grenoble, France*
[c]*Agefpi, LGP2, F-38000 Grenoble, France*
[d]*Univ. Grenoble Alpes, 3SR Lab, F-38000 Grenoble, France*
[e]*CNRS, 3SR Lab, F-38000 Grenoble, France*
[f]*Univ. Grenoble Alpes, CERMAV, F-38000 Grenoble, France*
[g]*CNRS, CERMAV, F-38000 Grenoble, France*
† Present address: Univ. Lyon, LaMCoS, INSA-Lyon, CNRS UMR5259, F-69621, Lyon, France.

peculiar thermo-mechanical behavior is inherent to nanocomposites that are reinforced with slender cellulosic nanofibers and is usually attributed to the presence of a continuous and rigid network of NFCs connected through cohesive hydrogen bonds.[1,22,23]

In general, the elastic properties of NFC nanocomposites and nanopapers increase linearly with the NFC volume fraction ϕ.[3,24,25,26] Surprisingly, the elastic moduli of these materials are systematically lower than the theoretical predictions of most of the classical micromechanical models that were developed for fiber-reinforced polymer composites, papers or non-woven fabrics.[3,25,27,28] For example, Josefsson *et al.*[28] reported that various analytical micromechanical models, namely, classical laminate theory,[29] and the Tsai–Pagano,[30] Cox[31] and Krenchel[32] models, failed to predict the macroscale elastic properties of nanopapers. Using these models to estimate the NFC elastic moduli led to values that were much lower than those commonly reported in the literature.[33,34] Several factors could explain this discrepancy.

First, the dispersion of NFCs in polymer matrices has to be considered. Obtaining homogeneous dispersions of NFCs within polymer matrices is challenging and is the subject of intense research.[1,2] When introduced into non-polar media, NFCs exhibit a strong tendency for self-association due to the omnipresence of polar groups at their surface, namely hydroxyl (–OH) and carboxylates groups ($-COO^-$).[1,2,26] This effect is not taken into account in the previously mentioned models. The dispersion of NFCs in host polymers can be improved either by surface chemical modification of NFCs[35,36] or by using a surfactant compatibilizer.[37] Despite significant improvements made over the last few years, the most straightforward processing route to obtain homogeneous nanocomposites with a well-dispersed filler and high mechanical performances consists in using aqueous polymer dispersions and solutions.[20–22,24] This processing route generally enables the individualization of NFCs to be preserved. However, even using such favorable processing conditions, the resulting nanomaterials systematically exhibit lower mechanical performances compared with the predictions of the classical micromechanical models.[24]

In addition, NFC nanostructure descriptions have to be improved in analytical estimates. Observing the microstructures of nanocomposites and nanopapers is difficult. They are often characterized in 2D using AFM, SEM-FEG and TEM.[20,38,39,40] The overall orientation of NFCs can also be assessed using X-ray diffraction.[41] NFC networks in nanocomposite films or nanopapers are usually dense, layered and highly connected fibrous nanostructures[38,41] with pronounced planar NFC orientations. In addition, TEMPO-oxidized NFCs are wavy semi-crystalline nanofibers that display both straight segments and so-called kinks.[19,42,43] These two features are not taken into account in the previously mentioned models. Contrary to many classical micrometric fibrous systems, such as papers or non-woven fabrics,[44–46] it is very difficult to characterize and thus model the placements and orientations of NFCs in their networks as well as their connectivity, which is known to have an important role in the mechanical response of these materials. For other micrometric or nanometric fibrous systems where proper 3D images of the fibrous architectures are not available, analytical or numerical structure generators were developed to estimate the previously mentioned suitable descriptors.[27,47–51] For NFC-based materials, Kulachenko *et al.*[27] recently used a numerical generation procedure to evaluate the mechanical behavior of NFC nanopapers. However, the authors did not provide compact analytical descriptors to describe the fibrous nanostructures. More recently, we proposed[43] a semi-analytical model dedicated to NFC suspensions in which several nanoscale constitutive parameters, such as the connectivity, bonding area and the distance between the center of mass of interacting NFCs, were identified using realistic elementary volumes of the fibrous NFC nanostructures that were numerically generated.

Finally, the deformation mechanisms at the NFC scale are questionable. There is a lack of experimental data on the mechanical behavior of NFCs and the nature of the nanoscale forces transmitted between bonded NFCs and between NFCs and the surrounding polymer matrix (in the case of nanocomposites). However, several studies have provided useful information from direct or indirect experimental methods on the elastic modulus of several bundles of nanofibrils[33] using an AFM and nanoscale three-point bending tests. For proper testing conditions, the measured Young's moduli of NFC bundles were close to 90 GPa. In comparison with the Young's moduli reported in other studies[52,53] for crystalline cellulose, which ranged between 120 and 150 GPa, this lower value was attributed both to the bundle architecture of the sample and to the presence of amorphous regions. Using a similar experimental setup, Iwamoto *et al.*[34] reported a value of 145 GPa for the elastic modulus of single and highly crystalline TEMPO-oxidized fibrils that were extracted from tunicate. Few experimental studies assessed the stress transfer mechanisms. Recently, Raman spectroscopy was employed to measure the strain of NFCs at the molecular level in deformed nanocomposites and nanopapers.[54,55] For polylactic acid (PLA) nanocomposites reinforced with TEMPO-oxidized NFCs ($\phi \approx$ 0.1, 0.17 and 0.2), Bulota *et al.*[54] showed that, during tensile deformation, in the elastic regime, the nanoscale deformation of NFCs weakly depended on the NFC content ϕ and was close to the deformation exhibited in nanopapers prepared with the same NFCs. This interesting experimental result suggests that, for a wide range of NFC contents, the mechanics of NFC networks in polymer matrices is weakly affected by the presence of the matrix. In addition, Kulachenko *et al.*[27] brought additional information on the elastic properties of nanopapers using fine-scale numerical simulations. In particular, this study showed the major influence of the elastic deformations of both the NFC amorphous kinks and NFC bonds on the Young's modulus of nanopapers. However, this numerical model was not associated with any multiscale analytical framework.

In this context, the objective of this study is to develop from an experimental database, an analytical multiscale model for the prediction of the elastic properties of NFC-reinforced nanocomposites and nanopapers. The model takes into account (i) the tortuosity of TEMPO-oxidized NFCs and (ii) the spatially heterogeneous mechanical properties related to the semicrystalline regions and kinks of these particles. The model also takes into

account (iii) the complexity of the networks formed by NFCs and (iv) their associated deformation mechanisms. To establish some of the model assumptions and to validate its predictions, we first processed TEMPO-oxidized NFCs and then used them to prepare nanocomposites and nanopapers. To obtain homogeneous nanocomposites with well-dispersed NFCs we used a water-soluble polyethylene oxide (PEO) matrix which has high physico-chemical affinity with cellulose. From the analysis of TEM and AFM images and XRD patterns of NFCs and NFC-reinforced nanocomposites, realistic elementary volumes of the fibrous nanostructures were numerically generated. Several microstructural descriptors, such as the mean number of contacts per nanofiber, were determined. Combining these data with the numerical and experimental data available from the literature, relevant deformation mechanisms were assumed. Finally, the nanoscale mechanics was upscaled using a rigorous theoretical framework, namely, the homogenization with multiple scale asymptotic expansions for discrete structures, leading to an analytical expression for the stiffness tensors of NFC nanocomposites and nanopapers. This model provides insights into the origins of the low elastic properties of NFC nanocomposites and nanopapers.

2 Materials and methods

2.1 Extraction of NFCs

TEMPO-oxidized NFC suspensions (1 wt%) were prepared from a commercial eucalyptus bleached kraft pulp (Celbi, Portugal) using the extraction procedure already reported by Martoïa *et al.*[56] The as-prepared NFC suspensions were at pH 8.

2.2 Nanocomposite processing

Polyethylene oxide (PEO) with a viscosity average molecular weight M_v of 1 000 000 (Sigma Aldrich, France) was first dissolved in deionized water to obtain a 1 wt% solution. Then, various amounts of NFC suspensions were added into the PEO solutions to prepare PEO/NFC mixtures containing 0, 5, 10, 15, 20, 30, 40, 50, 60, 70, 80, 90, and 100 wt% of NFCs. The mixtures were homogenized (IKA T5, digital Ultra-Turrax) at 5000 rpm for 30 s and then placed in ultrasonic baths for 5 min to remove the air bubbles entrapped in the mixtures. Nanocomposite films were obtained by casting the mixtures in circular Teflon molds with 150 mm diameters and drying under a fume hood at room temperature ($T \approx 20$ °C).

The mean thickness of the films $e \approx 15-20$ μm was measured using a digital paper micrometer, and the basic weight W was determined by measuring the weight of 70 mm × 60 mm rectangular specimens of films. The volume fractions of NFC ϕ was calculated using the film density $\rho = W/e$ and the NFC mass fraction of each constituent x, *i.e.*, $\phi = x\rho/\rho_{NFC}$, with $\rho_{NFC} = 1500$ kg m^{-3}.[57]

2.3 Microstructure characterization

The surface of the nanocomposite films was observed using a Nanoscope III AFM (Veeco, Canada) operating in tapping mode with an OTESPA silicon cantilever (Bruker, USA) at different locations over scanning regions of 3 μm × 3 μm and 1.1 μm × 1.1 μm.

The microstructure of the nanocomposite films was observed by scanning electron microscopy (SEM). Some films were fractured after freezing in liquid nitrogen and surface-coated with a thin (2–3 nm) layer of Au/Pd. Secondary electron images of the film cross section were recorded in high vacuum using a Zeiss Ultra 55 microscope equipped with a field emission gun (FEG) and operating at 2 kV. Other films were embedded in Epon resin and the resulting blocks were surfaced with a diamond knife in a Leica Ultracut UC6 ultramicrotome in order to visualize the cross-section of the films. The blocks were observed in a low pressure of air (40 Pa) with a FEI Quanta-FEG 250 microscope operating at 3 kV.

Transmission electron microscopy (TEM) was used to characterize the NFC morphology. Droplets of a dilute (0.001 wt%) NFC suspensions were deposited onto glow-discharged carbon-coated copper grids and the specimens were negatively stained with 2% uranyl acetate. Ultrathin (50–70 nm) cross-sections of Epon-embedded strips of NFC films were cut at room temperature using a Leica Ultracut UC6 ultramicrotome and collected on carbon-coated TEM grids. All specimens were observed in a Philips CM200 microscope operating at 80 kV and the images were recorded on Kodak SO163 films.

The nanofibril orientation in the films was assessed by X-ray diffraction (XRD). Strips of cellulose films were fixed on a 0.2 mm collimator in such a way that they were oriented parallel or perpendicular to the X-ray beam. The specimens were X-rayed in transmission mode in a vacuum chamber with a Ni-filtered CuKα radiation ($\lambda = 0.1542$ nm), using a Philips PW3830 generator operating at 30 kV and 20 mA. Two-dimensional diffraction patterns were recorded on Fujifilm imaging plates, read with a Fujifilm BAS-1800II bioimaging analyzer.

2.4 Mechanical characterization

Uniaxial tensile tests were performed on rectangular specimens (mean width ≈4 mm and mean initial length $l_0 \approx 40$ mm) at a constant strain-rate $\dot{\varepsilon} = 0.01$ s^{-1} using an electromechanical testing machine (Instron 5960, France) equipped with a force sensor of 50 N. Before testing, nanocomposite films were stored for at least 1 day under controlled conditions: $T = 25$ °C and 56% relative humidity (r.h.). Thermomechanical measurements were conducted using a DMA (TA Instruments RSA3, USA) in tensile mode. The tests were performed at a constant frequency of 1 Hz and with a strain amplitude of 0.05% on rectangular specimens (mean width ≈4 mm and mean initial length $l'_0 \approx 10$ mm). The samples were heated from 300 to 450 K at 5 K min^{-1}.

3 Experimental results

3.1 Morphology of the processed NFCs

In a previous study[43,56] we showed that the processed TEMPO-oxidized NFC suspensions were stable and unflocculated at high pH and low ionic strength. In these colloidal systems, the stability is ensured by the presence of a high content of carboxylate groups [–COO$^-$] in the order of 1.45 mmol g^{-1}

introduced at the surface of NFCs during TEMPO-mediated oxidation.[56] We also showed using optical microscopy that the processed TEMPO-oxidized NFC suspensions did not exhibit pronounced birefringent textures.[43] The AFM and TEM micrographs in Fig. 1 revealed that the individualized nanofibers were randomly deposited onto the surface of the substrate after drying. The nanofibers did not self-assemble into well-ordered domains in water suspension or during drying. This was likely due to their very high aspect ratio and their tortuous shape with kinks.

The determination of the morphological characteristics of NFCs is the subject of intense research.[42] Here, several descriptors of the NFC geometry were estimated from TEM micrographs, as shown in Fig. 1b. We measured a mean NFC diameter d of approximately 4 nm and a mean NFC length l of approximately 1200 nm (based on the measurement of 100 and 15 NFCs, respectively), *i.e.*, a mean NFC aspect ratio $r = l/d \approx 300$. It is worth noting that these dimensions were on the same order of magnitude as those reported by Usov *et al.*[42] using AFM and TEM images from TEMPO-oxidized NFCs extracted from wood fibers. In addition, Fig. 1b shows that TEMPO-oxidized fibrils were tortuous and consisted of an assembly of approximately $n_{seg} = 7$ slender straight segments with a mean length of $l_{seg} \sim 171$ nm interspersed with kinks with a mean length of $l_a \approx d$. The mean misorientation angle θ_{seg} between each consecutive segment of an individual NFC was close to $\pi/8$ rad.[43]

3.2 Microstructure of NFC-reinforced nanocomposites and nanopapers

The AFM and SEM micrographs of the processed nanocomposites showed that the nanofibers were homogenously distributed in the PEO matrix (Fig. 2). Indeed, neither NFC aggregates nor sedimentation of the fibrous reinforcement were observed. In addition, the AFM micrographs of the surface of NFC-reinforced nanocomposites (Fig. 2a) and nanopapers (Fig. 3a) revealed that NFCs were entangled at the nanoscale. This was confirmed by the TEM image of an ultrathin cross-section of a nanopaper shown in Fig. 3d. The section briefly floated on water after ultramicrotomy, resulting in a partial disruption and swelling of the nanopaper fragment. Although the image is thus not strictly that of the multilayered organization, it is a good illustration of the dense network of highly connected NFCs. However, even using high-resolution imaging techniques, the observations of the fibrillar architecture and the presence of pores in the bulk of the materials still remains challenging.

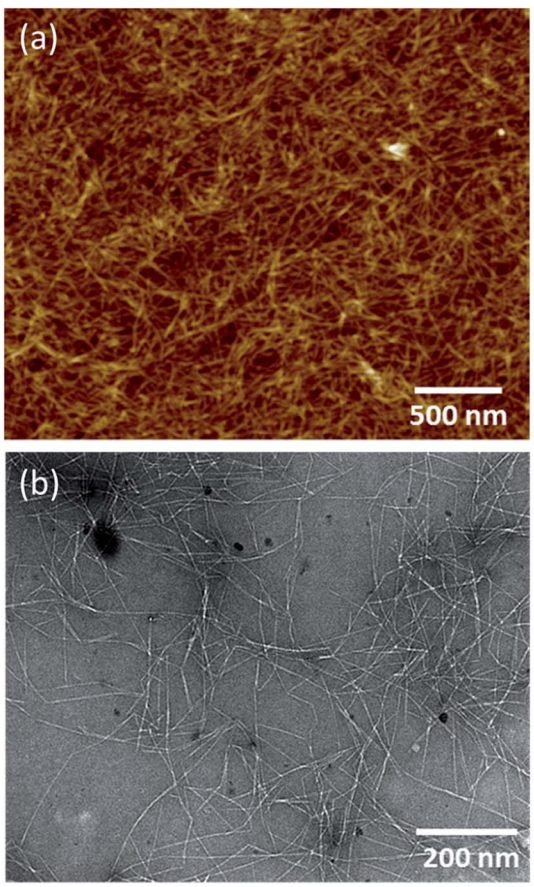

Fig. 1 AFM (a) and TEM (b) micrographs of TEMPO-oxidized NFCs after drying 0.01 wt% and 0.001 wt% suspensions, respectively. In (b), the NFCs were negatively stained.

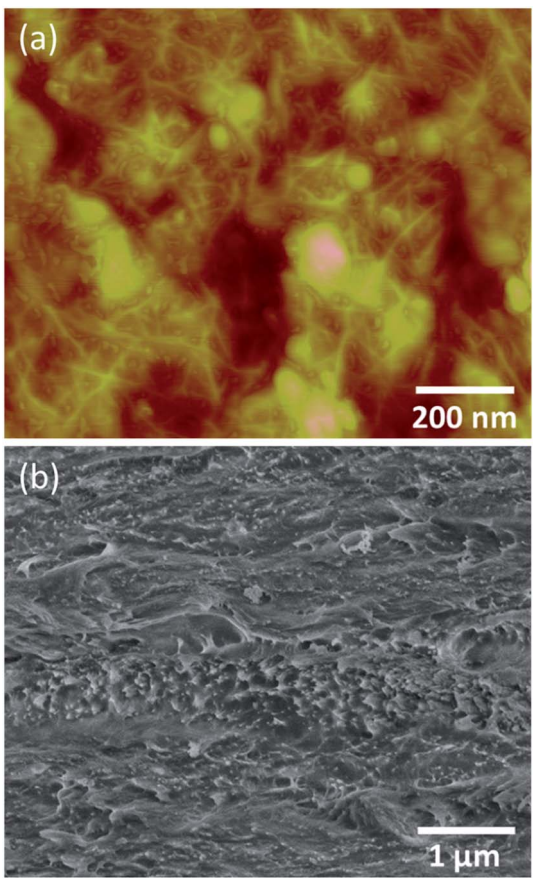

Fig. 2 (a) AFM micrograph of the surface of a nanocomposite film ($\phi = 0.14$); (b) SEM-FEG image of the cross-section of a fractured nanocomposite film ($\phi = 0.31$).

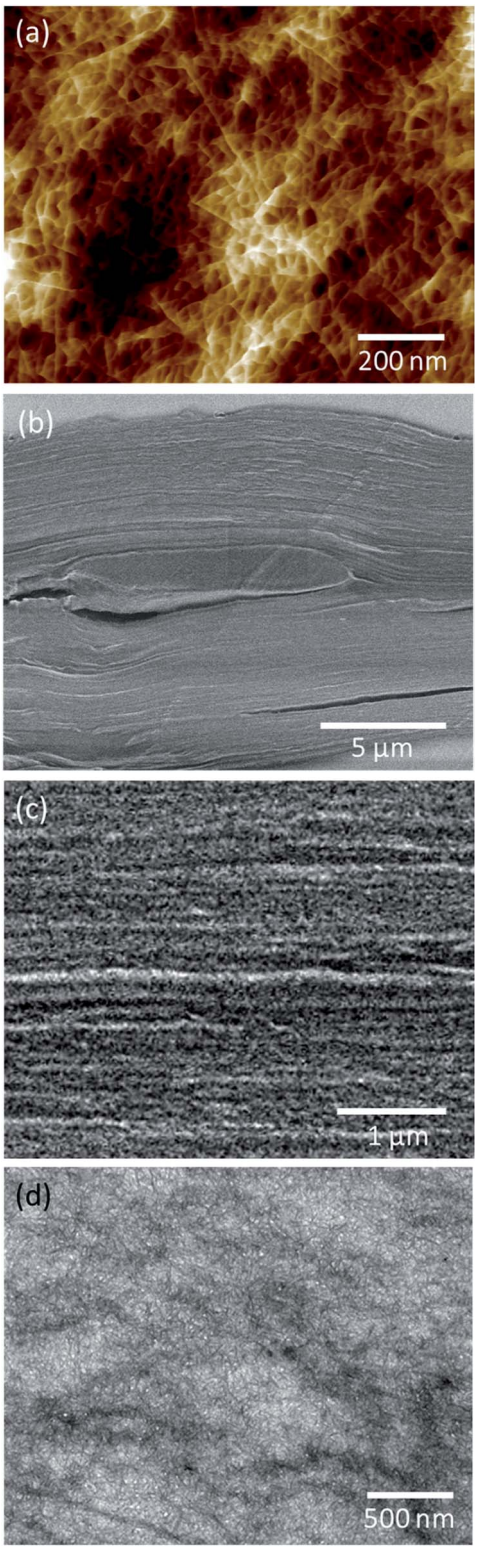

Fig. 3 (a) AFM micrograph of the surface of a TEMPO-oxidized NFC nanopaper. (b and c) SEM-FEG images of the cross-sections of a TEMPO-oxidized NFC nanopaper. In (b), the cross-section of a residual fiber can be seen. The few cracks in the film were likely induced by the cutting blade. (d) TEM micrograph of the ultrathin transverse section of the NFC nanopaper. During flotation of the ultrathin section on water, the film swelled to some extent and the multilayered organization was disrupted, revealing the intricate network of NFCs.

The overall orientation of the nanofibrils in the PEO/NFC nanocomposites with varying NFC contents ($0.11 \leq \phi \leq 0.93$) was evaluated by XRD diffraction (Fig. 4).[41] When the films were oriented perpendicular to the X-ray beam (left column in Fig. 4), most two-dimensional diffraction patterns were of powder nature, exhibiting a series of concentric rings. For $\phi = 0.11$, as expected, the pattern of PEO was dominant, characterized by two main strong diffraction rings, which showed that the PEO matrix was semicrystalline.[58,59] With increasing ϕ, the contribution of PEO in the pattern decreased and above $\phi = 0.8$, the pattern of cellulose was recognized. At $\phi = 0.8$, the PEO rings disappeared and the background intensity significantly increased. This suggests that the crystallization of PEO was somehow hindered by the large fraction of NFCs and affected by the constrained environment. At $\phi = 0.93$, the pattern is then typical of allomorph Iβ, characteristic of native wood cellulose, which exhibits five main diffraction rings corresponding to $(1\bar{1}0)$, (110), (102), and (200) and (004) planes of the crystal.[60] The rings in the pattern at $\phi = 0.93$ were not strictly homogeneous, which indicates that some weak orientation of the NFCs existed in the region probed by the X-ray beam. However, for all patterns, we considered that the NFCs were randomly oriented within the plane of the film.

When the films were oriented parallel to the X-ray beam (right column in Fig. 4), the patterns were of fiber nature, exhibiting distributions of more or less extended arcs. For $\phi = 0.11$ and 0.33, the PEO rings exhibited only a weak anisotropy, indicating that the crystallites were mostly randomly oriented in the film. For $\phi = 0.33$, the arcs corresponding to cellulose started to be visible with a higher intensity along the equator of the pattern. This anisotropic pattern was even clearer at higher NFC contents. For $\phi = 0.93$, the $1\bar{1}0$, 110, and 200 arcs were equatorial while the 004 reflection was meridional. Considering that the cellulose chains were parallel to the long axis of the NFCs as well as the *c*-axis of the unit cell, these fiber diffraction patterns confirm that most NFC were oriented in-plane in the film.[41] This is consistent with the layered texture which was observed in the SEM-FEG micrographs in Fig. 2b, 3b and 3c. The slight out-of-plane orientation (revealed by the arcing of the reflections) could be related to the presence of the few remaining partially disintegrated fibers, such as the one that was visible in the image of Fig. 3b, that distorted the planar organization in their vicinity.

Therefore, for the sake of simplicity, in the following, we considered that NFC nanopapers and nanocomposites could be regarded as mostly planar fibrous microstructures.

3.3 Mechanical properties

Fig. 5a shows that the elastic modulus E of the fabricated nanocomposites increased linearly with increasing nanofiber content ϕ. The variation of E with ϕ was nicely fitted using Cox's model for planar fibrous structures with random orientations, *i.e.*, with $E_{COX} = \phi E_{NFC}/3$.[31] However, this result was obtained for a irrealistic low value of the NFC Young's modulus of $E_{NFC} = 35$ GPa (Fig. 5a). This suggests that the elastic behavior of the studied nanocomposites and nanopapers is ruled by microstructures and elementary deformation micro-mechanisms

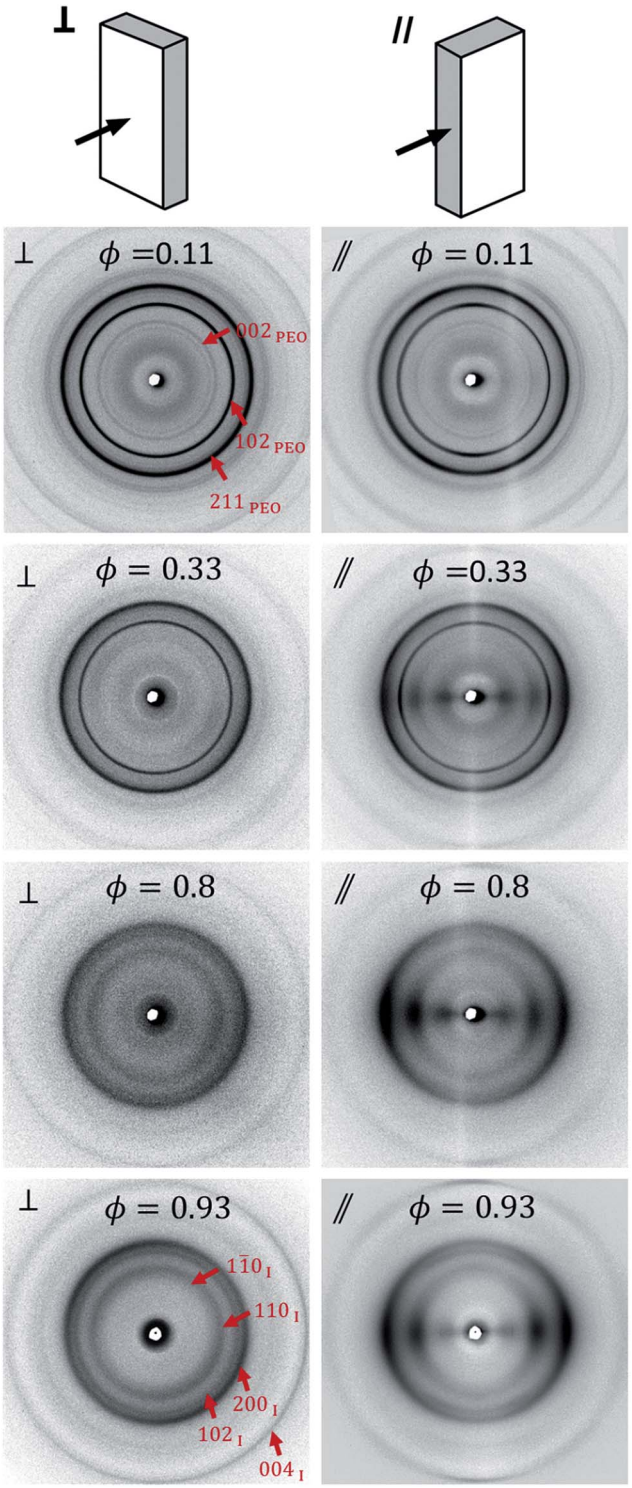

Fig. 4 X-ray diffraction patterns of nanocomposite films and nanopapers oriented perpendicular (left column) or parallel (right column) to the X-ray beam, for various NFC contents ϕ. In the right column, the films are vertical with respect to the XRD patterns. The arrows indicate the direction of the X-ray beam.

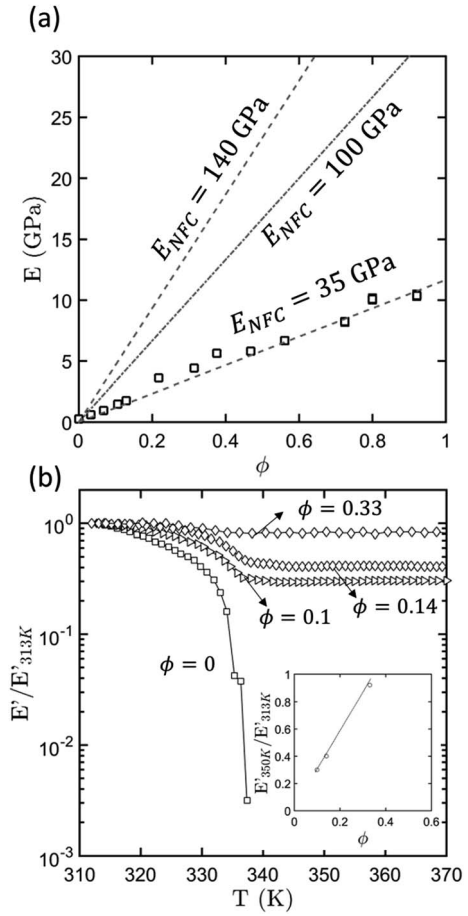

Fig. 5 (a) Evolution of the elastic modulus E as a function of the nanofiber content ϕ. The lines show the predictions of Cox's model for different values of NFC elastic moduli. (b) Normalized dynamic tensile modulus $E'/E'_{313\ K}$ as a function of the temperature at 1 Hz for various NFC-reinforced nanocomposites. The inset shows the evolution of the ratio $E'_{350\ K}/E'_{313\ K}$ as a function of ϕ.

different from those assumed in Cox's theory. Indeed, in the model proposed by Cox,[31] each fiber is straight and assumed to extend elastically from one side of the network to the other (elastic infinite bars), carrying only axial load and without interacting with neighboring fibers. As mentioned in the introduction, it is important to notice that the other well-known micromechanical models would also result in too low values of E_{NFC}, tending to prove that their assumptions do not fit the micromechanics of NFC networks in nanocomposites and nanopapers.[28]

The DMA curves in Fig. 5b provide evidence of the progressive thermal stabilization of the PEO matrix for $T > T_m = 338$ K with increasing the NFC content. The PEO matrix exhibited the typical behavior of a soft thermoplastic polymer: the dynamic modulus E' decreased with increasing temperature T before suddenly collapsing close to the melting temperature T_m = 338 K. Above this temperature the matrix exhibited a fluid-like behavior. The nanocomposites displayed a very different mechanical response: for $T < T_m$, the dynamic modulus E' was almost constant and then slightly decreased at $T = T_m$ before reaching a second plateau for $T \gg T_m$. In this situation, the material exhibited a solid-like behavior and did not flow even at very high temperature. This peculiar behavior is inherent to nanocomposites that are reinforced with a sufficient amount of

cellulosic nanofibers and is usually attributed to the presence of a continuous rigid network of NFCs connected *via* cohesive hydrogen bonds.[23] Hence, cohesive bonds between NFCs greatly contribute to the overall elastic response of the considered nanocomposites and nanopapers, even for low NFC contents.

4 Theory

From the experimental data gathered in the previous section and the difficulty of standard micromechanical models to predict the elastic behavior of NFC-based nanocomposites and nanopapers, we propose a novel analytical network model for the mechanics of these materials. The network model was built on several assumptions related both to the fibrous NFC architectures (Subsection 4.1) and deformation mechanisms at the NFC scale (Subsection 4.2). These elements were implemented in a theoretical upscaling technique (Subsection 4.3) in which additional kinematical assumptions were stated to obtain a compact and analytical estimate (Section 4.4).

4.1 Microstructure idealization

To draw a relevant picture of the NFC networks in the considered nanocomposites and nanopapers, the NFC geometrical parameters determined in Section 3, *i.e.* d, l, n_{seg}, l_{seg}, and θ_{seg}, were used in a numerical microstructure generation process similar to that reported by Martoïa *et al.*[43] Each tortuous nanofiber with i center of mass G^i was first randomly positioned in a representative elementary volume of size $V = 1400 \times 1400 \times 1400$ nm^3. Following this procedure, various fibrous networks with various nanofiber contents ϕ were generated with 3D random orientation of the nanofibers. Then, to mimic realistic planar NFC networks, each generated volume was numerically subjected to a simple compression test along the $\boldsymbol{e}_3$-direction. The evolution of the mean orientation vector $\mathbf{p}^i$ of each NFC i that progressively aligned in the ($\boldsymbol{e}_1$, $\boldsymbol{e}_2$)-plane was computed by solving a modified Jeffery's equation until a nearly planar NFC orientation was reached.[56] Fig. 6b shows an example of a typical idealized NFC network that was generated using this procedure ($\phi = 0.01$). This figure also shows the stereographic projection (pole figure of orientation) of vectors $\mathbf{p}^i$. In accordance with the XRD patterns shown in Fig. 4, the pole figure reveals the near-random distribution of the nanofibers along the ($\boldsymbol{e}_1$, $\boldsymbol{e}_2$)-plane. It is worth noting that other fibrous architectures (random, unidirectional with or without clustering) could also be obtained using this generation procedure.

The connectivity of the generated NFC networks was then assessed using a deterministic methodology based on a soft-core approach similar to that adopted in the statistical tube-model.[61] A cylindrical control volume Ω of size $V = \pi l_{seg} d^2$ centered on the centerline of the segment k belonging to a nanofiber i was defined. Each nanofiber segments l that belonged to a nanofiber j, the centerline of which intersected the control volume Ω, was added to the connectivity set of "hydrogen" bonds $\mathcal{B}^h$ contained in the representative volume Ω. We checked that this generation procedure yielded the prediction of the analytical tube model for straight nanofibers ($\theta_{seg} = 0$). In this case, the tube model prediction of the fiber coordination number Z^h, *i.e.*, the number of NFC bonds h per NFC, is

$$Z^h = 4\phi\left(\frac{2}{\pi} r\Phi_1 + \Phi_2 + 1\right), \quad (1)$$

where the discrete expressions for the orientation functions Φ_1 and Φ_2 are defined as follows:

$$\Phi_1 = \frac{1}{N^2}\sum_{i=1}^{N}\sum_{j=1}^{N}\|\mathbf{p}^i \otimes \mathbf{p}^j\| \text{ and } \Phi_2 = \frac{1}{N^2}\sum_{i=1}^{N}\sum_{j=1}^{N}\left|\mathbf{p}^i \cdot \mathbf{p}^j\right|, \quad (2)$$

where N is the number of NFCs in the representative volume.

Our numerical results revealed that the mean coordination number of the tortuous NFC Z^h could be well predicted analytically using eqn (1) with the orientation functions Φ_1 and Φ_2 calculated from the unit tangent vectors of the NFC segments (Fig. 6a). Regardless of the nanofiber content, Fig. 6c shows that the mean coordination number of the tortuous NFCs Z^h (continuous line) was slightly higher ($\approx$8%) than that expected for straight nanofibers (dashed line).

Some numerical studies[62] showed that a critical number of contacts $Z^h \approx 5$ is required to form fully connected planar networks without disjointed substructures. It is interesting to note that due to the pronounced slenderness of NFCs, *i.e.*, $r = 300$, Z^h was significantly higher than 5 for the investigated range of NFC contents: Z^h increased drastically from 16 for $\phi \approx 0.03$ up to $Z^h \approx 490$ in pure NFC nanopapers. This increase was in accordance with the evolution of the DMA curves (Fig. 5b), which showed the potential network-induced thermal stabilization of the polymer matrix. Thus, the considered NFC-based nanocomposites and nanopapers are highly connected fibrous materials in which contact micromechanics is a crucial parameter in the theoretical modeling (see below).

4.2 Micromechanical assumptions

From the previous experimental and numerical data, the elasticity of the NFC-based nanocomposites and nanopapers was interpreted in light of the NFC network mechanics, assuming that their properties were mainly governed by the fibrous architectures and their mechanics. This assumption was supported by the following observations:

- In the elastic domain, the mechanics of the NFC networks was weakly affected by the presence of the polymer matrix (see the previous comments in the introduction related to the study of Bulota *et al.*[54]).

- The elastic properties of the nanocomposites were, for a wide range of NFC contents (at least for $\phi > 0.3$), weakly affected by the temperature (even well beyond the melting temperature of the polymer matrix, Fig. 5b).

Therefore, to study the mechanics of the NFC networks and, consequently, the mechanics of the nanocomposites with equivalent nanofiber contents, it was assumed that NFCs were slender and kinked beams consisting of an average of $n_{seg} = 7$ straight and mostly crystalline rods linked by short less organized or damaged regions.[42] This idealization of the NFC geometry was supported by the study of Nishiyama *et al.*,[63] who reported, using small-angle neutron diffraction, that ramie

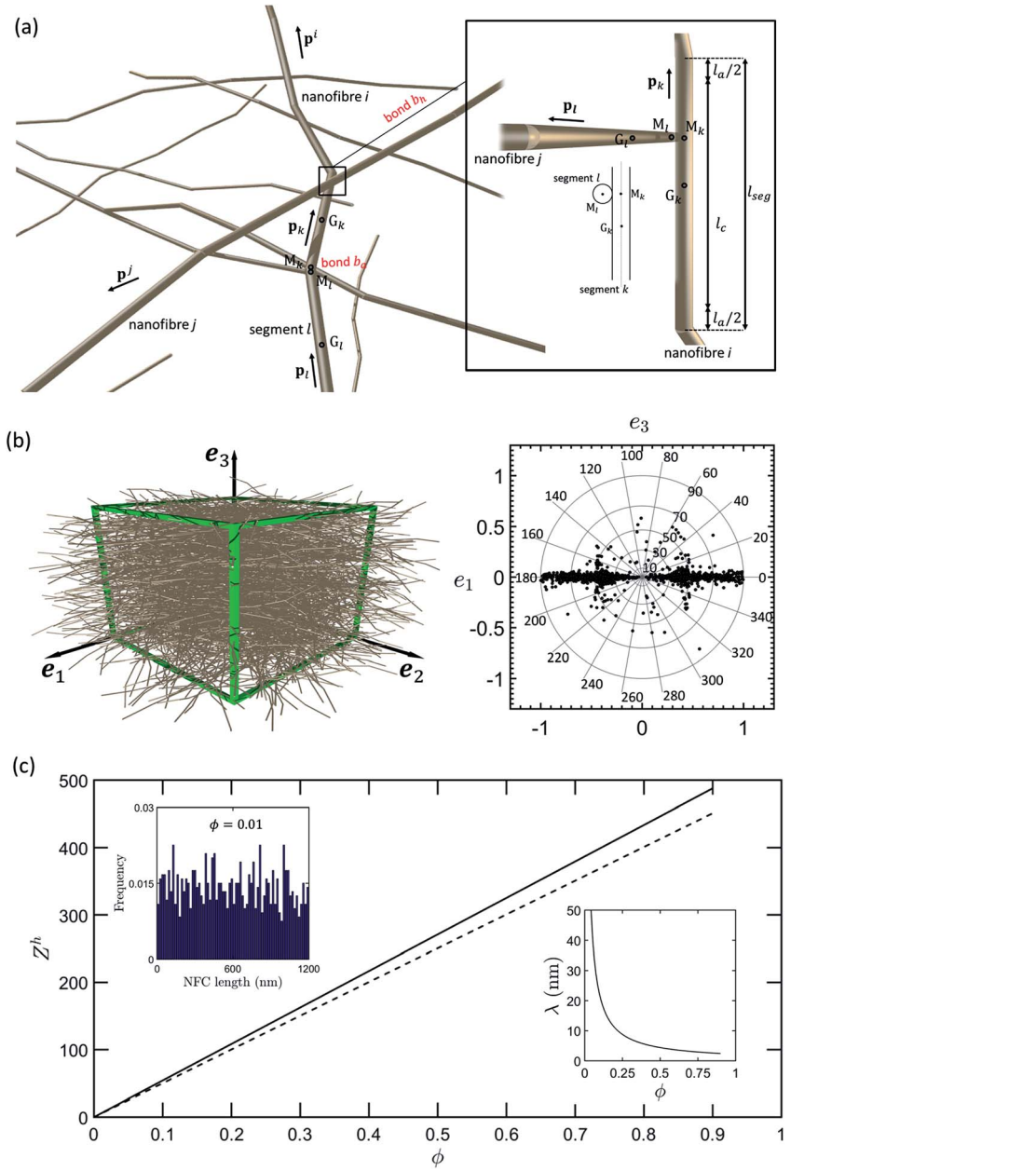

Fig. 6 (a) Idealized representation of interacting NFCs and zoom on an interaction bond. (b) Example of an idealized NFC network with a low nanofiber content $\phi = 0.01$ and with random planar orientation. The mean orientation vectors $\mathbf{p}^i$ of each tortuous NFC i were represented using a stereographic projection along the $\mathbf{e}_2$ direction. (c) Evolution of the mean coordination numbers Z^h as a function of the NFC volume fraction ϕ for fibrous networks of tortuous NFCs (continuous line). The dashed line is the prediction for straight nanofibers. The inset (on the right side) shows the evolution of the inter-contact distance $\lambda = l/(1 + Z^h)$ as a function of the NFC volume fraction ϕ. The histogram in inset shows that the NFC–NFC bonds were uniformly distributed along the NFC length.

fibrils exhibited quasi-periodic ordered-disordered regions along their length. The authors also revealed that the length of the ordered zones l_c was close to 150 nm ($l_c \approx 167$ nm in the fibril model in Fig. 6a). Accounting for the previously mentioned remarks, each kink (noted b_a in the following paragraphs) with a length $l_a \approx d$ was assumed to be an amorphous or disordered cellulose region. Hence, kinks (Fig. 6a) were assigned a mean elastic modulus of $E_a \approx 5$ GPa (ref. 64–66) and, assuming a Poisson ratio of $\nu = 0.3$, a mean shear modulus of $G_a \approx 1.9$ GPa. In contrast, the rods with a length $l_c \approx 167$ nm (Fig. 6a) were assumed to be ordered regions with a high crystallinity.[19] Thus, accounting for the theoretical evaluations and experimental measurements dedicated to cellulose crystals[66–69] that gave a longitudinal modulus of 150 GPa and a transverse modulus of 50 GPa, the semicrystalline rods of length $l_c \approx 167$ nm (Fig. 6a) were assigned, using the rule of mixture, a mean longitudinal elastic modulus of $E_c^l \approx 120$ GPa, a mean transverse modulus of $E_c^t \approx 40$ GPa and, assuming a transverse

Poisson ratio of $\nu \approx 0.3$, a mean transverse shear modulus of $G_c^t \approx 19$ GPa. These estimates are in agreement with the predictions of the elastic properties of the semicrystalline parts of cellulose nanofibrils using fine scale numerical simulation,[66,69,70] showing that the contrast between the shear modulus of disordered and ordered regions is at least of one order of magnitude.

It has already been reported in many theoretical and numerical studies dealing with the mechanics of papers[71] and NFC nanopapers[27] that the elastic deformations of the fiber-to-fiber bond regions also play significant roles in their elasticity. In accordance with these studies, it was assumed that NFCs were connected through rod–rod elastic bonds b_h (Fig. 6a).

While subjecting such idealized NFC networks (Fig. 6b) to macroscopic mechanical loadings, each inter-contact NFC segment could be stretched, sheared, bent and twisted.[72] Likewise, at $\phi = 0.5$, the length λ of the semicrystalline rod segments and the length l_a of kinks were practically equal (Fig. 6c). Thus, as the elastic properties of the semicrystalline rod segments were ten times higher than those of amorphous regions, it was reasonable to assume that their deformation was negligible compared with that of amorphous kinks. At higher NFC contents, this assumption was even more valid because the length of the semicrystalline rod segments decreased (Fig. 6c), and consequently, their stiffness increased. Thus, at least for $\phi \geq 0.5$, the micromechanics was reduced to the problem of quasi-rigid beams, namely, the semicrystalline rodlike segments linked by amorphous kinks or bonds b_a and hydrogen bonds b_h in each NFC–NFC contact zone. This scenario will be adopted in the following section. Below $\phi = 0.5$, its validity becomes questionable.

Under such circumstances, when the considered fibrous networks were subjected to a macroscopic displacement gradient $\nabla\mathbf{U}$, the infinitesimal displacement $\mathbf{u}_k^{M_k}$ of a point M_k of a rod k (belonging to a nanofiber i) located at a curvilinear abscissa s_k from its center of mass G_k along the rod centerline of tangent unit vector $\mathbf{p}_k$ ($\mathbf{G}_k\mathbf{M}_k = s_k\mathbf{p}_k$) was written as follows:

$$\mathbf{u}_k^{M_k} = \mathbf{u}_k + s_k\mathbf{w}_k \times \mathbf{p}_k, \tag{3}$$

where $\mathbf{u}_k$ is the infinitesimal displacement of G_k and $\mathbf{w}_k$ the rotation of the rod k.

The displacements and rotation of the rods induced the deformation of both the kinks b_a and the rod–rod bonds b_h. Hence, it is assumed that the deformations of bonds b_a and b_h mainly induced shear reaction forces $\mathbf{f}_a$ and $\mathbf{f}_h$ and reaction moments $\mathbf{m}_a$ and $\mathbf{m}_h$, respectively. Phenomenological generic linear expressions for $\mathbf{f}_\alpha$ and $\mathbf{m}_\alpha$ (where the subscript "α" stands either for kink bonds "a" or rod–rod contact bonds "h") were proposed as follows:

$$\mathbf{f}_\alpha = K_\alpha\Delta\mathbf{u}_\alpha, \tag{4}$$

and

$$\mathbf{m}_\alpha = K'_\alpha\Delta\mathbf{w}_\alpha, \tag{5}$$

with $\Delta\mathbf{u}_\alpha$ and $\Delta\mathbf{w}_\alpha$ the infinitesimal relative displacement and rotation of the connected rods k and l:

$$\Delta\mathbf{u}_\alpha = \mathbf{u}_k - \mathbf{u}_l + \Delta\mathbf{w}_\alpha \times (s_k\mathbf{p}_k - s_l\mathbf{p}_l), \tag{6}$$

$$\Delta\mathbf{w}_\alpha = \mathbf{w}_k - \mathbf{w}_l. \tag{7}$$

The translational K_α and rotational K'_α bond stiffnesses were assumed to be linear and quadratic functions of the representative descriptors of the bond cross sections S_α ($K_\alpha = k_\alpha S_\alpha$ and $K_\alpha = k'_\alpha {S_\alpha}^2$), respectively. A suitable descriptor of S_a is typically $\pi d^2/4$, *i.e.*, the cross sectional circular area of the amorphous kinks, whereas S_b is often considered to be proportional to the rhomb surface[73,74] defined by the projection of the connected rods (k and l) onto the normal plane of the bonding zone $d^2/\mathbf{p}_k \times \mathbf{p}_l$.

Hence, by introducing $\mathcal{B}_k^\alpha$, *i.e.*, the set of bonds b_α of rod k, the momentum balance that governs the quasi-static motion of a given rod k was expressed as follows:[74,75]

$$\begin{cases} \displaystyle\sum_{\mathcal{B}_k^a} \mathbf{f}_a + \sum_{\mathcal{B}_k^h} \mathbf{f}_h = 0 \\ \displaystyle\sum_{\mathcal{B}_k^a} \mathbf{m}_a + \sum_{\mathcal{B}_k^h} \mathbf{m}_h = \sum_{\mathcal{B}_k^a} s_k^a \mathbf{f}_a \times \mathbf{p}_k + \sum_{\mathcal{B}_k^h} s_k^h \mathbf{f}_h \times \mathbf{p}_k \end{cases}. \tag{8}$$

4.3 Theoretical upscaling

There is a close analogy between the micromechanical problem presented in the above section and that developed by Le Corre *et al.*[74,75] to model the rheology of highly concentrated fiber bundle suspensions with planar bundle orientation and Newtonian bundle–bundle interactions. To be convinced of this, the present elastic interactions b_α and the infinitesimal displacement and rotation fields of the rods could be replaced by the viscous interactions and the translational and rotational velocity fields of the bundles in the suspensions that were studied by Le Corre *et al.*[74,75] To study the nature and the properties of the equivalent continuous medium related to this type of micromechanics, the authors used the homogenization method for discrete structures with multiscale asymptotic expansions.[76] They showed[74,76] that, under good scale separation conditions, *i.e.* when the macroscale size of the studied fibrous materials was much larger than the fiber length (this condition is largely fulfilled with the investigated nanocomposites), the local reaction forces $\mathbf{f}_\alpha$ typically kept their generic form (eqn (4)). In addition, the relative infinitesimal displacement $\Delta\mathbf{u}_\alpha$ in eqn (6) could be approximated at the first order by

$$\Delta\mathbf{u}_\alpha \approx \delta\mathbf{u}_k - \delta\mathbf{u}_l + \nabla\mathbf{U}\cdot\boldsymbol{\xi}_\alpha + \mathbf{w}_l \times s_l\mathbf{p}_l - \mathbf{w}_k \times s_k\mathbf{p}_k, \tag{9}$$

where $\delta\mathbf{u}_k$ and $\delta\mathbf{u}_l$ are the first order displacement fluctuations around the macroscopic displacement field $\mathbf{U}$ and where $\boldsymbol{\xi}_\alpha = \mathbf{G}_k\mathbf{G}_l = s_k\mathbf{p}_k - s_l\mathbf{p}_l$.

The homogenization method[74,76] also showed that, under these conditions, the equivalent macroscale continuum is a standard Cauchy medium with a macroscale symmetric stress tensor $\boldsymbol{\sigma}$ that takes the following generic discrete form:

$$\boldsymbol{\sigma} = \frac{1}{V}\sum_{\mathcal{B}_k^{\mathrm{a}}} \boldsymbol{\xi}_{\mathrm{a}} \otimes \mathbf{f}_{\mathrm{a}} + \frac{1}{V}\sum_{\mathcal{B}_k^{\mathrm{h}}} \boldsymbol{\xi}_{\mathrm{h}} \otimes \mathbf{f}_{\mathrm{h}}, \tag{10}$$

where V is the volume of the representative elementary volume. By introducing $B^{\alpha}/V = n_{\mathrm{seg}} n z^{\alpha}/2$, the number of α-bonds per unit volume and n the number of nanofibers per unit volume N/V (z^{α} is the number of bonds b_{α} per segment), $\boldsymbol{\sigma}$ can be finally expressed as follows:

$$\boldsymbol{\sigma} = k_{\mathrm{a}} z^{\mathrm{a}} \frac{\pi d^2 n_{\mathrm{seg}} n}{8} \frac{1}{B^{\mathrm{a}}} \sum_{\mathcal{B}_k^{\mathrm{a}}} \boldsymbol{\xi}_{\mathrm{a}} \otimes \Delta u_{\mathrm{a}} + k_{\mathrm{h}} z^{\mathrm{h}} \frac{d^2 n_{\mathrm{seg}} n}{2} \frac{1}{B^{\mathrm{h}}} \sum_{\mathcal{B}_k^{\mathrm{h}}} \frac{1}{\|p_k \times p_l\|} \boldsymbol{\xi}_{\mathrm{h}} \otimes \Delta u_{\mathrm{h}}. \tag{11}$$

Still using the homogenization method,[74,76] it was shown that the first order fluctuations $\delta\mathbf{u}_k$ and $\mathbf{w}_k$ are linear functions of the macroscale displacement gradient $\nabla\mathbf{U}$ and that $\boldsymbol{\sigma}$ is a linear function of the macroscale strain tensor $\boldsymbol{\varepsilon} = (\nabla\mathbf{U} + \nabla\mathbf{U}^{\mathrm{t}})/2$:

$$\boldsymbol{\sigma} = (\mathbb{C}^{\mathrm{a}} + \mathbb{C}^{\mathrm{h}}) : \boldsymbol{\varepsilon}, \tag{12}$$

where $\mathbb{C}^{\mathrm{a}}$ and $\mathbb{C}^{\mathrm{h}}$ are the symmetric macroscopic elastic stiffness tensors related to kink bonds and segment–segment bonds, respectively.

4.4 Analytical estimates

Two strategies can be used to estimate the value of the components of the stiffness tensors, $\mathbb{C}^{\mathrm{a}}$ and $\mathbb{C}^{\mathrm{h}}$. The first strategy would consist in solving, *e.g.*, using discrete element simulations,[75,77] the mechanical equilibrium of the representative elementary volumes, such as that shown in Fig. 2b, when subjected to macroscopic displacement gradients $\nabla\mathbf{U}$. The second strategy, which was used in this study, led to analytical estimates of $\mathbb{C}^{\mathrm{a}}$ and $\mathbb{C}^{\mathrm{h}}$ from additional assumptions both on the NFC nanostructures and kinematics. These assumptions are described below:

• It was assumed that eqn (1) gave a proper prediction of the mean coordination number Z^{h}. It was also assumed that the segment–segment bonds were uniformly distributed along the NFC length, so that $z^{\mathrm{h}} = Z^{\mathrm{h}}/n_{\mathrm{seg}}$ (see the inset in Fig. 6c). In addition, z^{a} was easily deduced from n_{seg}: $z^{\mathrm{a}} = 2(n_{\mathrm{seg}} - 1)/n_{\mathrm{seg}}$.

• The two terms inside the summation of eqn (11) were assumed to be weakly correlated, so that $1/\|\mathbf{p}_k \times \mathbf{p}_l\|$ was extracted from the summation and approximated by its mean value $1/\overline{\|p_k \times p_l\|}$.

$$\overline{S}_{\mathrm{h}} = \frac{d^2}{\|\mathbf{p}_k \times \mathbf{p}_l\|} \approx \frac{d^2}{\varphi_1} \tag{13}$$

where $\varphi_1 = \dfrac{1}{{N_{\mathrm{seg}}}^2}\displaystyle\sum_{k=1}^{N_{\mathrm{seg}}}\sum_{l=1}^{N_{\mathrm{seg}}} \|\mathbf{p}_k \otimes \mathbf{p}_l\|$ with $N_{\mathrm{seg}} = n_{\mathrm{seg}} N$.

• The infinitesimal displacement field $\mathbf{u}_k$ of rod k was assumed to be an affine function of the macroscopic displacement gradient $\nabla\mathbf{U}$. This assumption led to neglecting the first right-hand term in the expression of $\Delta\mathbf{u}_{\alpha}$, *i.e.*, $\delta\mathbf{u}_k - \delta\mathbf{u}_l \approx 0$. By performing discrete element simulations to compute the effective elastic properties of papers, Marulier[77] showed that this approximation practically led to the same results.

• The rotation of the rod k noted $\mathbf{w}_k \times \mathbf{p}_k$ was assumed to follow that subjected by the macroscale transformation. This can be expressed as follows:

$$\mathbf{w}_k \times \mathbf{p}_k = \nabla\mathbf{U}\cdot\mathbf{p}_k - \mathbf{p}_k \otimes \mathbf{p}_k \otimes \mathbf{p}_k : \boldsymbol{\varepsilon}. \tag{14}$$

Thus, accounting for the two previous assumptions, $\Delta\mathbf{u}_{\alpha}$ was rewritten:

$$\Delta\mathbf{u}_{\alpha} = (s_k \mathbf{p}_k \otimes \mathbf{p}_k \otimes \mathbf{p}_k - s_l \mathbf{p}_l \otimes \mathbf{p}_l \otimes \mathbf{p}_l) : \boldsymbol{\varepsilon}. \tag{15}$$

Finally, after some analytical developments, detailed in Appendix, a simple and compact analytical estimate of the stiffness tensor $\mathbb{C} = \mathbb{C}^{\mathrm{a}} + \mathbb{C}^{\mathrm{h}}$ was obtained:

$$\mathbb{C} = \left(k_{\mathrm{a}} \frac{\pi}{8}(n_{\mathrm{seg}} - 1) + k_{\mathrm{h}} Z^{\mathrm{h}} \frac{1}{12\varphi_1}\left(1 - \frac{n_{\mathrm{seg}}}{Z^{\mathrm{h}}}\right)\right) n d^2 {l_{\mathrm{seg}}}^2 \mathbb{A}, \tag{16}$$

where $\mathbb{A}$ is the fourth-order rod orientation tensor defined as[78]:

$$\mathbb{A} = \frac{1}{N_{\mathrm{seg}}}\sum_{k=1}^{N_{\mathrm{seg}}} \mathbf{p}_k \otimes \mathbf{p}_k \otimes \mathbf{p}_k \otimes \mathbf{p}_k. \tag{17}$$

In particular, when nanopapers and nanocomposites are subjected to a tensile loading, eqn (16) led to the following expression of the Young's modulus E:

$$E = \left(k_{\mathrm{a}} \frac{\pi}{8}(n_{\mathrm{seg}} - 1) + k_{\mathrm{h}} Z^{\mathrm{h}} \frac{1}{12\varphi_1}\left(1 - \frac{n_{\mathrm{seg}}}{Z^{\mathrm{h}}}\right)\right) n d^2 {l_{\mathrm{seg}}}^2 \left(A_{1111} - \frac{A_{2211}}{A_{2222}} A_{1122}\right), \tag{18}$$

where A_{1111}, A_{2211}, A_{2222} and A_{1122} are the components of the fourth-order orientation tensor that are determined using the numerical microstructure generation process presented in Subsection 4.1.

Eqn (18) shows the role played by the NFC geometry (l_{seg}, d, n_{seg}), content ($n = 4\phi/(d^2 l)$), and orientation ($\mathbb{A}$, φ_1) as well as the key role played by the bond stiffnesses (k_{a}, k_{h}) on the macroscale elastic modulus of NFC-based nanocomposites and nanopapers. It also shows the importance of having a relevant representation of the NFC nanostructures to properly estimate the connectivity Z^{h} (Section 4.1).

5 Model prediction and discussion

To complete the description of the NFC geometry and architecture, the bond stiffnesses k_{a} and k_{h} were the only remaining parameters of the model to be determined. A first order estimate of the shear stiffness of the kinks k_{a} is $G_{\mathrm{a}}/l_{\mathrm{a}}$. By introducing this estimate into eqn (19), the macroscale amorphous contribution E_{a} to the overall Young's modulus E was estimated. This contribution is shown in Fig. 7. Similarly, with the knowledge of E_{a}, the bond stiffness k_{h} was estimated from the best fit of the overall Young's modulus E to the experimental data. We found that $k_{\mathrm{h}} = 7.44 \times 10^{15}$ N m^{-3}. This led to the

macroscale contribution E_h plotted in Fig. 7 from which several important remarks can be drawn.

• A nice fit of the experimental data was obtained using the analytical estimate of the elastic modulus E of nanocomposites and nanopapers (eqn (18)). Surprisingly, the model prediction was still satisfactory below the model validity domain, *i.e.*, below $\phi = 0.5$.

• The model prediction shows that the kinks played an important role in the elasticity of the studied NFC nanocomposites and nanopapers. In the validity domain of the model, *i.e.*, above $\phi = 0.5$, E_a represents 98% to 73% of E as the NFC content varied from 0.5 to 0.9. In addition, E_a increased linearly with ϕ. This trend can be explained from eqn (16) because E_a is a linear function of $n = 4\phi/(d^2 l)$.

• The contribution of NFC–NFC bonds to the elastic properties was lower but could not be neglected. The contribution E_h to the elastic modulus E was a power-law function of ϕ with an exponent of 2. As shown in eqn (16), E_h is a function of nZ^h, where n and Z^h are both linear functions of the nanofiber content ϕ.

• The value of k_h led to an overall bond stiffness $K_h = 0.09$ N m^{-1}. This estimate was compared with the stiffness K_h^* that would correspond to a full and perfect bonding region with typical size $\bar{S}_h$. A reasonable estimate of $K_h^* = G_c^t d = 62$ N m^{-1} was obtained by considering the simple shear of such perfect bonding region between the centerlines of two contacting NFCs. The origin of the important difference between K_h and K_h^* could be related to the irregular geometry[42] of bonds, as NFCs do not exhibit rectangular cross sections. As already been observed in other cellulose fibrous materials,[45,79] the effective bonding area can be much smaller than $\bar{S}_h$. For example, by closely analyzing the 3D microstructures of unbeaten bleached softwood papers, Marulier *et al.*[45,76] showed that the effective bond surface area was approximately 10% of the full contact area $\bar{S}_h$. Another origin of this discrepancy could result from inefficient physicochemical bonding mechanisms at the interfaces between contacting NFCs,[38,77]. These two scenarios could be coupled. Additional fine scale observations and characterizations as well as molecular dynamics simulations would contribute to a better understanding of the potential mechanisms at the origin of this discrepancy.

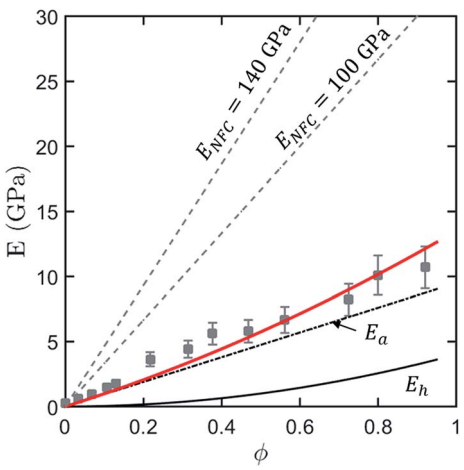

Fig. 7 Young's modulus E of the fabricated films as a function of the NFC content ϕ. The continuous red line shows the prediction of the micromechanical model stated in eqn (18). The other black lines represent the contributions that are induced by the kink bonds E_a (dash-dotted line) and NFC–NFC bonds E_h (continuous line). The fits were obtained using an equivalent bond stiffness of 7.44×10^{15} N m^{-3}. The mean experimental values were assigned a relative deviation of 15%. The grey dashed lines are the prediction of Cox's model.

• Further, the significance the NFC–NFC bond stiffness k_h was investigated in regards of the stored energy per unit surface area E_h in the bonds. This energy was roughly estimated as $E_h \approx \frac{1}{2} k_h \Delta\bar{u}^2$, where $\Delta\bar{u}$ is the average relative displacement in the bond region between two interacting NFCs. It was estimated from eqn (15) as follows $\Delta\bar{u} \approx \left(\frac{l_{seg}}{4}\right)^2 \varepsilon^2$ with ε the tensile macroscopic tensile strain. Hence, by considering a tensile strain at breakage of $\varepsilon_r \approx 4\%$ for the nanopaper, E_h was approximately 0.2×10^{-22} kJ nm^{-2}. As reported in the literature, the energy at breakage of paper bonds between cellulose fibers[80,81] or between model cellulose films[82] ranges between 0.5 $\times 10^{-22}$ kJ nm^{-2} and 1×10^{-22} kJ nm^{-2}. These bonds are brittle and thus these energies at breakage can be considered to roughly correspond to elastic energies, showing that our estimate for the stiffness of NFC–NFC bond properties is reasonable.

• The stiffness of the amorphous zone k_a was estimated by assuming that shear was the main deformation mechanism that occurred in these zones and that their effective cross section was close to S_a. These assumptions have to be regarded carefully because the deformation mechanisms and kink nanostructures could be extremely complex.[42,83] Once again, fine scale experimental characterization[83] and molecular dynamics simulations[84,85] would enable a proper understanding of the geometry and mechanics of kinks.

6 Conclusion

The objective of this study was to relate the macroscale elasticity of NFC-reinforced polymer nanocomposites and NFC nanopapers to their complex nanostructures and deformation mechanisms. Nanocomposite films made of TEMPO-oxidized NFCs and a water soluble polymer matrix of polyethylene oxide (PEO) were fabricated by casting with various NFC contents that ranged from 0 to 100 wt%. The nanostructure of the nanocomposites was studied using AFM, TEM, SEM-FEG and XRD, showing that NFCs formed intricate planar fibrous networks, in agreement with the literature data. Tensile tests showed that their elastic moduli increased linearly as a function of the nanofiber content ϕ. In addition, DMA tests showed a progressive thermal stabilization of the polymer matrix with increasing NFC content. This particular thermomechanical behavior was attributed to the presence of a continuous and rigid network of NFC connected through cohesive hydrogen bonds.

Therefore, to better understand the nanostructure of NFC nanocomposites and nanopapers, we first proposed an idealized nanofibril model built from several geometrical parameters that were estimated using TEM images. In particular, NFCs were described as kinked and slender nanofibers with alternating rodlike semicrystalline segments linked by short less organized regions. A numerical generator of NFC networks was used to obtain realistic elementary volumes of planar nanostructures with randomly oriented NFCs. This procedure enabled several suitable descriptors of NFC-based materials to be determined. For example, in the experimental range of NFC contents, *i.e.*, $0.03 \leq \phi \leq 0.92$, the mean coordination number of the tortuous NFCs Z^{h} was shown to range between 16 and 490, suggesting that the micromechanics of NFC–NFC bonds have to be considered for proper modeling of the mechanical properties of these materials.

In this context, an original multiscale model was developed to predict the elastic properties of NFC nanocomposites and nanopapers, in which the shear of NFC–NFC bonds and kink bonds in NFC-based materials was the governing deformation mode. In this approach, the deformation was assumed to be localized at the numerous NFC–NFC interfaces between NFCs and in the less organized NFC regions, whereas the semicrystalline NFC regions were considered to be rigid bodies because of their high intrinsic stiffness compared with the kink zones. Furthermore, the role of the polymer matrix was reasonably neglected. The upscaling approach was based on the theoretical framework of the homogenization with multiscale asymptotic expansions for discrete structures. A compact and simple analytical expression for the stiffness tensor of NFC nanocomposites and nanopapers was established. The local stiffness of the kink bond regions and the NFC–NFC bonds were determined using the experimental database and the numerically generated NFC nanostructures. The results showed the predominant role played by the amorphous or damaged kinks on the elastic properties. The contribution of the NFC–NFC bonds was significant for the highest NFC contents. The NFC–NFC bond stiffness was very low compared with the theoretical estimate of this property, assuming a simple shear of a perfect bonding region between contacting NFCs. Irregular and partial bonding surface areas as well as poor physicochemical interfacial bonding mechanisms could explain these low values.

The developed original modeling approach provides a practical framework and offers new possibilities for optimizing the structural, mechanical properties of NFC nanopapers and NFC nanocomposites. Furthermore, the developed approach could easily be extended to the prediction of the mechanical and physical properties, *e.g.* the thermal or electrical properties, of a broad family of nanopapers and nanocomposites reinforced with nanofibers, such as carbon nanotubes, or graphene.[86–88]

However, it would be very interesting to verify the relevance of the approach using for instance other model systems (*e.g.*, highly crystalline NFCs produced from bacteria, algae or tunicates, monodisperse carbon nanotubes) or varying the overall orientation of nanofibers within the polymer matrix.[41] In addition, the model could be refined with further experimental investigation and simulations to improve the description of the geometry[83,89] and mechanics[85] of NFCs and NFC–NFC bonds.

Appendix

Accounting for all the assumptions stated in Section 4.4, the macroscale stress tensor $\boldsymbol{\sigma}$ eqn (11) could easily be expressed as follows:

$$\boldsymbol{\sigma} = \left(k_{\mathrm{a}} z^{\mathrm{a}} \frac{\pi d^2 n_{\mathrm{seg}} n}{8} \left(\mathbb{B}_1^{\mathrm{a}} + \mathbb{B}_2^{\mathrm{a}} \right) + k_{\mathrm{h}} z^{\mathrm{h}} \frac{d^2 n_{\mathrm{seg}} n}{2\varphi_1} \left(\mathbb{B}_1^{\mathrm{h}} + \mathbb{B}_2^{\mathrm{h}} \right) \right) : \boldsymbol{\varepsilon}, \tag{19}$$

where

$$\begin{cases} \mathbb{B}_1^{\alpha} = \dfrac{1}{B^{\alpha}} \displaystyle\sum_{N_{\mathrm{seg}}} \sum_{\mathcal{B}_k^{\alpha}} {s_k}^2 \mathbf{p}_k \otimes \mathbf{p}_k \otimes \mathbf{p}_k \otimes \mathbf{p}_k \\ \mathbb{B}_2^{\alpha} = \dfrac{1}{B^{\alpha}} \displaystyle\sum_{N_{\mathrm{seg}}} \sum_{\mathcal{B}_k^{\alpha}} s_k s_l \mathbf{p}_l \otimes \mathbf{p}_k \otimes \mathbf{p}_k \otimes \mathbf{p}_k \end{cases}, \tag{20}$$

The case of the rod–rod bonds b_{h} was considered separately from the case of amorphous kink bonds b_{a}, to simplify the expression of the tensors $\mathbb{B}_i^{\alpha}$.

Case of rod–rod bonds b_{h}

By assuming that rod–rod bonds were uniformly distributed along the rod length (see inset in Fig. 6(c)), the following discrete sums can be written:[90]

$$\begin{cases} \displaystyle\sum_{\mathcal{B}_k^{\mathrm{h}}} {s_k}^2 \approx z^{\mathrm{h}} \frac{{l_{\mathrm{seg}}}^2}{12} \left(1 - \frac{1}{z^{\mathrm{h}}} \right) \\ \displaystyle\sum_{\mathcal{B}_k^{\mathrm{h}}} s_k \approx 0 \end{cases}. \tag{21}$$

Then, by assuming that s_k and s_l are uncorrelated, the expressions of $\mathbb{B}_1^{\mathrm{h}}$ and $\mathbb{B}_2^{\mathrm{h}}$ are

$$\begin{cases} \mathbb{B}_1^{\mathrm{h}} \approx \dfrac{{l_{\mathrm{seg}}}^2}{6} \left(1 - \dfrac{1}{z^{\mathrm{h}}} \right) \mathbb{A} \\ \mathbb{B}_2^{\mathrm{h}} \approx 0 \end{cases}, \tag{22}$$

where $\mathbb{A}$ is the fourth-order rod orientation tensor defined in eqn (17). These two relations were validated using the microstructure generator.

Case of amorphous kink bonds b_{a}

In this particular case, bonds are systematically located at the extremities of the rods, so that

$$\forall k,\ {s_k}^2 = {l_{\mathrm{seg}}}^2/4, \tag{23}$$

and

$$\sum_{\mathcal{B}_k^{\mathrm{a}}} {s_k}^2 \approx z^{\mathrm{a}} \frac{{l_{\mathrm{seg}}}^2}{4} \ \text{ and } \ \mathbb{B}_1^{\mathrm{a}} \approx \frac{{l_{\mathrm{seg}}}^2}{2} \mathbb{A}, \tag{24}$$

and we also checked that $\mathbb{B}_2^a \approx 0$ using the microstructure generator.

Acknowledgements

This research was made possible thanks to the facilities of the TekLiCell platform funded by the Région Rhône-Alpes (ERDF: European regional development fund). LGP2 and 3SR laboratories are parts of the LabEx Tec 21 (Investissements d'Avenir – grant agreement no. ANR-11-LABX-0030) and of the Énergies du Futur and PolyNat Carnot Institutes (Investissements d'Avenir – grant agreements no. ANR-11-CARN-007-01 and ANR-11-CARN-030-01. The authors gratefully acknowledge the electron microscopy facility of the NanoBio-ICMG Chemistry Platform for granting access to its equipment and W. W. Sampson from the University of Manchester for fruitful discussions.

References

1 A. Dufresne, *Nanocellulose: From Nature to High Performance Tailored Materials*, Walter de Gruyter, 2013.
2 I. Siró and D. Plackett, *Cellulose*, 2010, **17**, 459–494.
3 K.-Y. Lee, Y. Aitomäki, L. A. Berglund, K. Oksman and A. Bismarck, *Compos. Sci. Technol.*, 2014, **105**, 15–27.
4 S. J. Eichhorn, A. Dufresne, M. Aranguren, N. E. Marcovich, J. R. Capadona, S. J. Rowan, C. Weder, W. Thielemans, M. Roman, S. Renneckar, W. Gindl, S. Veigel, J. Keckes, H. Yano, K. Abe, M. Nogi, A. N. Nakagaito, A. Mangalam, J. Simonsen, A. S. Benight, A. Bismarck, L. A. Berglund and T. Peijs, *J. Mater. Sci.*, 2009, **45**, 1–33.
5 R. J. Moon, A. Martini, J. Nairn, J. Simonsen and J. Youngblood, *Chem. Soc. Rev.*, 2011, **40**, 3941–3994.
6 C.-N. Wu, Q. Yang, M. Takeuchi, T. Saito and A. Isogai, *Nanoscale*, 2013, **6**, 392–399.
7 H. Zhu, S. Parvinian, C. Preston, O. Vaaland, Z. Ruan and L. Hu, *Nanoscale*, 2013, **5**, 3787–3792.
8 J. Huang, H. Zhu, Y. Chen, C. Preston, K. Rohrbach, J. Cumings and L. Hu, *ACS Nano*, 2013, **7**, 2106–2113.
9 M. Miao, J. Zhao, X. Feng, Y. Cao, S. Cao, Y. Zhao, X. Ge, L. Sun, L. Shi and J. Fang, *J. Mater. Chem. C*, 2015, **3**, 2511–2517.
10 C. Aulin, G. Salazar-Alvarez and T. Lindström, *Nanoscale*, 2012, **4**, 6622–6628.
11 M.-C. Hsieh, C. Kim, M. Nogi and K. Suganuma, *Nanoscale*, 2013, **5**, 9289–9295.
12 Z. Shi, G. O. Phillips and G. Yang, *Nanoscale*, 2013, **5**, 3194–3201.
13 R. Bardet, M. N. Belgacem and J. Bras, *Cellulose*, 2013, **20**, 3025–3037.
14 S. Saini, N. Belgacem, J. Mendes, G. Elegir and J. Bras, *ACS Appl. Mater. Interfaces*, 2015, **7**, 18076–18085.
15 J.-L. Wertz, J. P. Mercier and O. Bédué, *Cellulose Science and Technology*, CRC Press, 2010.
16 H. P. S. Abdul Khalil, Y. Davoudpour, M. N. Islam, A. Mustapha, K. Sudesh, R. Dungani and M. Jawaid, *Carbohydr. Polym.*, 2014, **99**, 649–665.
17 T. Saito, S. Kimura, Y. Nishiyama and A. Isogai, *Biomacromolecules*, 2007, **8**, 2485–2491.
18 A. Isogai, T. Saito and H. Fukuzumi, *Nanoscale*, 2011, **3**, 71–85.
19 A. Isogai, *J. Wood Sci.*, 2013, **59**, 449–459.
20 F. Dalmas, J.-Y. Cavaillé, C. Gauthier, L. Chazeau and R. Dendievel, *Compos. Sci. Technol.*, 2007, **67**, 829–839.
21 X. Xu, F. Liu, L. Jiang, J. Y. Zhu, D. Haagenson and D. P. Wiesenborn, *ACS Appl. Mater. Interfaces*, 2013, **5**, 2999–3009.
22 V. Favier, H. Chanzy and J. Y. Cavaillé, *Macromolecules*, 1995, **28**, 6365–6367.
23 V. Favier, J. Y. Cavaillé, G. R. Canova and S. C. Shrivastava, *Polym. Eng. Sci.*, 1997, **37**, 1732–1739.
24 H. Sehaqui, Q. Zhou and L. A. Berglund, *Soft Matter*, 2011, **7**, 7342–7350.
25 C. J. G. Plummer, S. Galland, F. Ansari, Y. Leterrier, P.-E. Bourban, L. A. Berglund and J. E. Månson, *Plast. Rubber Compos.*, 2015, **44**, 81–86.
26 C. J. G. Plummer, C. K. C. Choo, C. I. R. Boissard, P.-E. Bourban and J.-A. E. Månson, *Colloid Polym. Sci.*, 2013, **291**, 2203–2211.
27 A. Kulachenko, T. Denoyelle, S. Galland and S. B. Lindström, *Cellulose*, 2012, **19**, 793–807.
28 G. Josefsson, G. Chinga-Carrasco and E. K. Gamstedt, *RSC Adv.*, 2015, **5**, 58091–58099.
29 S. W. Tsai, *Theory of Composites Design*, Think composites, Dayton, Ohio, 1992.
30 S. W. Tsai and N. J. Pagano, *Invariant properties of composites materials*, Technomic Publishing, Stamford, Conn., 1968.
31 H. L. Cox, *Br. J. Appl. Phys.*, 1952, **3**, 72–79.
32 H. Krenchel, *Fibre Reinforcement*, Akademisk Forlag, Copenhagen, 1964.
33 Q. Cheng, S. Wang and D. P. Harper, *Composites, Part A*, 2009, **40**, 583–588.
34 S. Iwamoto, W. Kai, A. Isogai and T. Iwata, *Biomacromolecules*, 2009, **10**, 2571–2576.
35 A. Gandini and M. N. Belgacem, The Surface and In-Depth Modification of Cellulose Fibers, in *Cellulose Chemistry and Properties: Fibers, Nanocelluloses and Advanced Materials*, ed. O. J. Rojas, Springer International Publishing, 2016.
36 K. Missoum, M. N. Belgacem and J. Bras, *Materials*, 2013, **6**, 1745–1766.
37 L. Heux, G. Chauve and C. Bonini, *Langmuir*, 2000, **16**, 8210–8212.
38 A. J. Benítez, J. Torres-Rendon, M. Poutanen and A. Walther, *Biomacromolecules*, 2013, **14**, 4497–4506.
39 T. Saito, T. Uematsu, S. Kimura, T. Enomae and A. Isogai, *Soft Matter*, 2011, **7**, 8804–8809.
40 S. Fujisawa, T. Ikeuchi, M. Takeuchi, T. Saito and A. Isogai, *Biomacromolecules*, 2012, **13**, 2188–2194.
41 H. Sehaqui, N. Ezekiel Mushi, S. Morimune, M. Salajkova, T. Nishino and L. A. Berglund, *ACS Appl. Mater. Interfaces*, 2012, **4**, 1043–1049.
42 I. Usov, G. Nyström, J. Adamcik, S. Handschin, C. Schütz, A. Fall, L. Bergström and R. Mezzenga, *Nat. Commun.*, 2015, **6**, 7564.

43 F. Martoïa, P. J. J. Dumont, L. Orgéas, M. N. Belgacem and J.-L. Putaux, *Soft Matter*, 2016, **12**, 1721–1735.
44 J. Viguié, P. Latil, L. Orgéas, P. J. J. Dumont, S. Rolland du Roscoat, J.-F. Bloch, C. Marulier and O. Guiraud, *Compos. Sci. Technol.*, 2013, **89**, 202–210.
45 C. Marulier, P. J. J. Dumont, L. Orgéas, S. R. du Roscoat and D. Caillerie, *Cellulose*, 2015, **22**, 1517–1539.
46 L. Orgéas, P. J. J. Dumont, J.-P. Vassal, O. Guiraud, V. Michaud and D. Favier, *J. Mater. Sci.*, 2011, **47**, 2932–2942.
47 V. Favier, R. Dendievel, G. Canova, J. Y. Cavaillé and P. Gilormini, *Acta Mater.*, 1997, **45**, 1557–1565.
48 F. Dalmas, R. Dendievel, L. Chazeau, J.-Y. Cavaillé and C. Gauthier, *Acta Mater.*, 2006, **54**, 2923–2931.
49 L. Berhan and A. M. Sastry, *Phys. Rev. E*, 2007, **75**, 041121.
50 S. Lavrykov, S. B. Lindström, K. M. Singh and B. V. Ramarao, *Nord. Pulp Pap. Res. J.*, 2012, **27**, 256.
51 L. I. Salminen, M. J. Alava, S. Heyden, P.-J. Gustafsson and K. J. Niskanen, *Nord. Pulp Pap. Res. J.*, 2002, **17**, 105–110.
52 I. Sakurada, Y. Nukushina and T. Ito, *J. Polym. Sci.*, 1962, **57**, 651–660.
53 T. Nishino, K. Takano and K. Nakamae, *J. Polym. Sci., Part B: Polym. Phys.*, 1995, **33**, 1647–1651.
54 M. Bulota, S. Tanpichai, M. Hughes and S. J. Eichhorn, *ACS Appl. Mater. Interfaces*, 2012, **4**, 331–337.
55 S. Tanpichai, W. W. Sampson and S. J. Eichhorn, *Composites, Part A*, 2014, **65**, 186–191.
56 F. Martoïa, C. Perge, P. J. J. Dumont, L. Orgéas, M. A. Fardin, S. Manneville and M. N. Belgacem, *Soft Matter*, 2015, **11**, 4742–4755.
57 L. Salmén and C. Fellers, *J. Pulp Pap. Sci.*, 1989, **15**, J63–J65.
58 S. Liu, Y. Yin and H. Chen, *CrystEngComm*, 2013, **15**, 5853–5859.
59 M. Pereda, N. E. Kissi and A. Dufresne, *ACS Appl. Mater. Interfaces*, 2014, **6**, 9365–9375.
60 A. D. French, *Cellulose*, 2014, **21**, 885–896.
61 S. Toll, *J. Rheol.*, 1993, **37**, 123–125.
62 G. E. Pike and C. H. Seager, *Phys. Rev. B: Condens. Matter Mater. Phys.*, 1974, **10**, 1421–1434.
63 Y. Nishiyama, U.-J. Kim, D.-Y. Kim, K. S. Katsumata, R. P. May and P. Langan, *Biomacromolecules*, 2003, **4**, 1013–1017.
64 R. J. Hill, *Biomacromolecules*, 2008, **9**, 2963–2966.
65 S. J. Eichhorn and R. J. Young, *Cellulose*, 2001, **8**, 197–207.
66 K. Kulasinski, S. Keten, S. V. Churakov, D. Derome and J. Carmeliet, *Cellulose*, 2014, **21**, 1103–1116.
67 M. Bergenstråhle, L. A. Berglund and K. Mazeau, *J. Phys. Chem. B*, 2007, **111**, 9138–9145.
68 K. Tashiro and M. Kobayashi, *Polym. Bull.*, 1985, **14**, 213–218.
69 X. Wu, R. J. Moon and A. Martini, *Cellulose*, 2012, **20**, 43–55.
70 F. L. Dri, L. G. Hector Jr, R. J. Moon and P. D. Zavattieri, *Cellulose*, 2013, **20**, 2703–2718.
71 K. Niskanen, *Mechanics of Paper Products*, Walter de Gruyter, 2012.
72 J. A. Åström, J. P. Mäkinen, M. J. Alava and J. Timonen, *Phys. Rev. E*, 2000, **61**, 5550–5556.
73 P. Latil, L. Orgéas, C. Geindreau, P. J. J. Dumont and S. Rolland du Roscoat, *Compos. Sci. Technol.*, 2011, **71**, 480–488.
74 S. Le Corre, D. Caillerie, L. Orgéas and D. Favier, *J. Mech. Phys. Solids*, 2004, **52**, 395–421.
75 S. Le Corre, P. Dumont, L. Orgéas and D. Favier, *J. Rheol.*, 2005, **49**, 1029–1058.
76 J.-L. Auriault, *Int. J. Eng. Sci.*, 1991, **29**, 785–795.
77 C. Marulier, Etude multi-échelles des couplages entre propriétés hygroélastiques des papiers et leur microstructure, PhD thesis, University of Grenoble Alpes, 2013.
78 S. G. Advani and C. L. T. Iii, *J. Rheol.*, 1987, **31**, 751–784.
79 C. Marulier, P. J. J. Dumont, L. Orgéas, D. Caillerie and S. Rolland du Roscoat, *Nord. Pulp Pap. Res. J.*, 2012, **27**, 245.
80 U. Hirn and R. Schennach, *Sci. Rep.*, 2015, **5**, 10503.
81 F. J. Schmied, C. Teichert, L. Kappel, U. Hirn, W. Bauer and R. Schennach, *Sci. Rep.*, 2013, **3**, 2432.
82 S. Rohm, U. Hirn, C. Ganser, C. Teichert and R. Schennach, *Cellulose*, 2013, **21**, 237–249.
83 P. N. Ciesielski, J. F. Matthews, M. P. Tucker, G. T. Beckham, M. F. Crowley, M. E. Himmel and B. S. Donohoe, *ACS Nano*, 2013, **7**, 8011–8019.
84 C. H. Haigler, M. J. Grimson, J. Gervais, N. Le Moigne, H. Höfte, B. Monasse and P. Navard, *PLoS One*, 2014, **9**, e93981.
85 S. Paavilainen, T. Róg and I. Vattulainen, *J. Phys. Chem. B*, 2011, **115**, 3747–3755.
86 H. Lu, F. Liang, Y. Yao, J. Gou and D. Hui, *Composites, Part B*, 2014, **59**, 191–195.
87 L. Berhan, Y. B. Yi, A. M. Sastry, E. Munoz, M. Selvidge and R. Baughman, *J. Appl. Phys.*, 2004, **95**, 4335–4345.
88 R. Jung, H.-S. Kim, Y. Kim, S.-M. Kwon, H. S. Lee and H.-J. Jin, *J. Polym. Sci., Part B: Polym. Phys.*, 2008, **46**, 1235–1242.
89 J. Majoinen, J. S. Haataja, D. Appelhans, A. Lederer, A. Olszewska, J. Seitsonen, V. Aseyev, E. Kontturi, H. Rosilo, M. Österberg, N. Houbenov and O. Ikkala, *J. Am. Chem. Soc.*, 2014, **136**, 866–869.
90 J.-P. Vassal, L. Orgéas, D. Favier, J.-L. Auriault and S. Le Corre, *Phys. Rev. E*, 2008, **77**, 011303.